Prediction of unconventional magnetism in doped FeSb$_2$

Igor I. Mazin[a,b,1,2] , Klaus Koepernik[c], Michelle D. Johannes[d], Rafael González-Hernández[e,f], and Libor Šmejkal[f,g,1]

[a]Department of Physics and Astronomy, George Mason University, Fairfax, VA 22030; [b]Center for Quantum Science and Engineering, George Mason University, Fairfax, VA 22030; [c]Institute for Theoretical Solid State Physics, Leibniz Institute for Solid State and Materials Research Dresden, 01 069 Dresden, Germany; [d]Center for Computational Materials Science, Naval Research Laboratory, Washington, DC 20375; [e]Grupo de Investigación en Física Aplicada, Departamento de Física, Universidad del Norte, 081002 Barranquilla, Colombia; [f]Institut für Physik, Johannes Gutenberg Universität Mainz, 55 128 Mainz, Germany; and [g]Institute of Physics, Czech Academy of Sciences, 162 00 Praha 6, Czech Republic

It is commonly believed that the energy bands of typical collinear antiferromagnets (AFs), which have zero net magnetization, are Kramers spin-degenerate. Kramers nondegeneracy is usually associated with a global time-reversal symmetry breaking (e.g., via ferromagnetism) or with a combination of spin–orbit interaction and broken spatial inversion symmetry. Recently, another type of spin splitting was demonstrated to emerge in some collinear magnets that are fully spin compensated by symmetry, nonrelativistic, and not even necessarily noncentrosymmetric. These materials feature nonzero spin density staggered in real space as seen in traditional AFs but also spin splitting in momentum space, generally seen only in ferromagnets. This results in a combination of materials characteristics typical of both ferromagnets and AFs. Here, we discuss this recently discovered class with application to a well-known semiconductor, FeSb$_2$, and predict that with certain alloying, it becomes magnetic and metallic and features the aforementioned magnetic dualism. The calculated energy bands split antisymmetrically with respect to spin-degenerate nodal surfaces rather than nodal points, as in the case of spin–orbit splitting. The combination of a large (0.2-eV) spin splitting, compensated net magnetization with metallic ground state, and a specific magnetic easy axis generates a large anomalous Hall conductivity ($\sim$150 S/cm) and a sizable magnetooptical Kerr effect, all deemed to be hallmarks of nonzero net magnetization. We identify a large contribution to the anomalous response originating from the spin–orbit interaction gapped anti-Kramers nodal surfaces, a mechanism distinct from the nodal lines and Weyl points in ferromagnets.

antiferromagnetism | altermagnetism | anomalous Hall effect | magnetooptics | first principles calculations

Antiferromagnets (AFs) are associated with spin-degenerate bands throughout the entire Brillouin zone (BZ). The reason is that while AFs do break the time-reversal symmetry $\mathcal{T}$ microscopically, they preserve it overall, by definition, when combined with another symmetry operation $\mathcal{O}$. Examples of such operations are a lattice translation t (i.e., doubling of the unit cell) or a spatial inversion $\mathcal{P}$. These combined symmetries protect the Kramers spin degeneracy for all wave vectors. Recently, it has been pointed out that this is not universally the case. There exist magnets wherein the collinear spin densities (we do not discuss noncollinear spin textures in this paper) are perfectly compensated, but their particular spatial anisotropy leads to a strong spin splitting of energy bands (1–6) and surprisingly strong anomalous responses such as spontaneous crystal Hall effect (1, 7, 8), crystal magnetooptical Kerr effect (9), spin-polarized currents (10, 11), and giant magnetoresistance effects (8, 12, 13). The materials base for this emerging class of magnets is potentially large, but so far, relatively few materials have been convincingly identified (1, 7), and we have only started to explore the consequences of their fascinating electronic structure. In addition, many of these systems are insulating, which

eliminates or strongly suppresses many of the interesting effects above, while others have a ground-state easy axis incompatible with the anomalous response.

To satisfy the conditions necessary to realize this unconventional magnetism, there must be more than one crystallographically equivalent magnetic site in the nonmagnetic unit cell (otherwise, the operation $\mathcal{O}$ would be a lattice translation). Furthermore, the structure should not contain any bonds connecting ions with opposite spins such that their middle point is an inversion symmetry center; otherwise, the result is an ordinary AF with Kramers degeneracy since such an operation would map a spin-up state onto a spin-down state with the same momentum. Incidentally, the same condition is usually invoked for the Dzyaloshinskii–Moriya interaction.

One way to break this symmetry is to surround magnetic ions with tilted cages of nonmagnetic atoms (1) such as in the marcasite structure. Arguably, the best-explored marcasite material is FeSb$_2$, which is experimentally nonmagnetic, although it exhibits unusual magnetic response properties including a change from diamagnetic to paramagnetic. Experimentally, the FeSb$_2$ transport switches from weakly semiconducting at higher temperatures to metallic at $T \sim 50$ to 100 K. The optical gap has

Significance

For many decades, it has been commonly believed that all electronic states of a collinear antiferromagnet (AF) are spin-degenerate, unless the underlying crystal structure lacks centrosymmetry and has spin–orbit coupling. This has been essentially definitional for antiferromagnetism and is widely used experimentally to distinguish ferromagnets from AFs. Recently, it was demonstrated that a new class of magnets, possessing antiferromagnetic order and without net magnetization but showing a typical ferromagnetic response in many aspects, is possible. We predict that FeSb$_2$, which is well known but poorly understood magnetically, is an incipient unconventional magnet of this type and can be pushed to become one by Co or Cr doping. Moreover, the calculated magnetic anisotropy is favorable for exhibiting various anomalous properties.

been measured to be between 76 (14) and 130 meV (15), and the transport gap is anisotropic with multiple gaps between 4 and 36 meV (14–16). Various density functional theory (DFT)–based calculations (17–19) have found a pseudogap or a semi-conducting nonmagnetic state with an indirect gap. Although all transport measurements confirm the semiconducting state, angular-resolved photoemission measurements detect metallic states, attributed to surface states of a correlated topological nature (20). The nonmagnetic gapped state, however, is calculated to have a trivial topological character, and the magnetic state has bands in strong qualitative disagreement (not simple renormalization) with the measured dispersion. Thus, FeSb$_2$ in its stoichiometric state is characterized as an "exotic insulator" (20). Doping with both Cr (21) and Co (22) has been realized and does lead to observed magnetic phases, some of them not entirely characterized.

In this paper, we predict, using first principles calculations, that stoichiometric FeSb$_2$ is, on the mean-field level, an ordinary AF with standard Kramers degenerate bands and adopts the structure traditionally called AFMe (using notations from ref. 27) as shown in Fig. 1A. However, our calculations show that this structure is nearly degenerate with a different magnetic structure, AFMo (Fig. 1B), which is an unconventional "dual" magnet as described above. Because the calculated energy of the nonmagnetic (NM) state is also nearly degenerate with both the AFMe and AFMo magnetic states, we argue that the lowest-energy antiferromagnetic state shown in Fig. 1A is suppressed in the stoichiometric compound due to spin fluctuations. Importantly, all three energies (NM, AFMe, and AFMo) are close

Fig. 1. Magnetic ground states in FeSb$_2$. The Kramers (A) and spin-split (B) ordering shown on the FeSb$_2$ structure. Fe atoms are shown in red ("up" spin) and blue ("down" spin), and Sb atoms are shown in light gray. In the Kramers state, we mark the half-unit cell translation coupled with time reversal $\mathbf{t}\mathcal{T}$. In the AFMo state, we mark the inversion symmetry $\mathcal{P}$. (C) Top view along the c axis on the spin-polarized Fermi surface calculated for the spin-split antiferromagnetic FeSb$_2$ state. (D) BZ with special points; colored planes indicate marked spin-degenerate AK nodal surfaces. We also show the paths ΓR and $\Gamma R'$ to emphasize that it is orbitally degenerate but with an opposite spin polarization (marked by green and orange), and we mark the magenta $\mathcal{R}_S \mathcal{M}_x$ plane.

despite the fact that the AFMo structure, being a good metal, is disadvantaged by kinetic energy. Not surprisingly, then, when this disadvantage is removed by doping FeSb$_2$ away from the semiconducting gap, the unconventional spin-split AFMo state is stabilized; this is the case for moderate hole (Cr) or electron (Co) doping. Larger dopings stabilize the trivial AFMe structure.

The nonrelativistic band structure of the AFMo phase exhibits spin-split Fermi surfaces as illustrated in Fig. 1C, with nodal planes as shown in Fig. 1D. The spin splitting follows a higher symmetry than the underlying orthorhombic crystal structure since reflection across these planes changes the sign but not the amplitude of the splitting. It can therefore be expanded into lattice harmonics as

$$E(\boldsymbol{k}, \uparrow) - E(\boldsymbol{k}, \downarrow) = F(\boldsymbol{k}) \sin(k_x a) \sin(k_y b), \qquad [1]$$
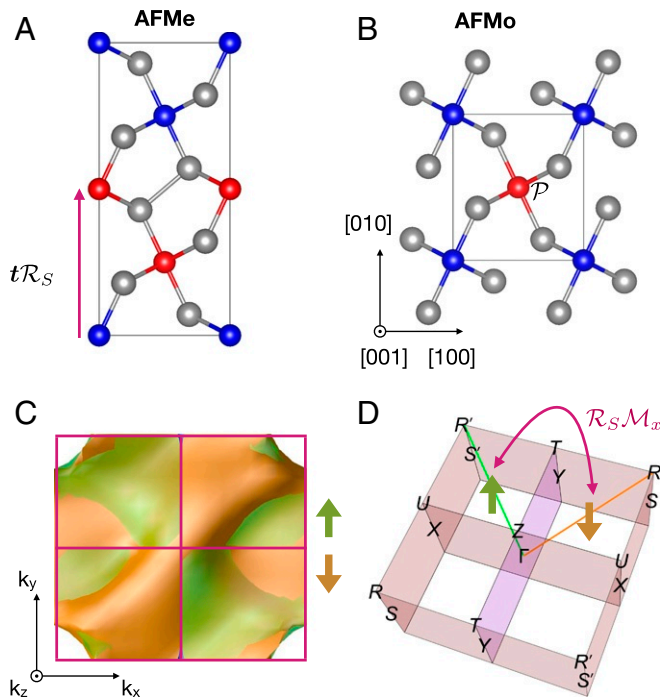
where $F(\boldsymbol{k})$ respects the full underlying lattice symmetry and a and b are the lattice parameters. We refer to the resulting symmetrically spin-split band structure with Kramers nodal surfaces as anti-Kramers (AK) to distinguish it from the conventional Rashba antisymmetric spin splitting with spin-degenerate Kramers points. Furthermore, we show by direct relativistic first principles calculations that the spin–orbit interaction gapped AK nodal surfaces significantly contribute to a large spontaneous crystal Hall conductivity $\sigma_{xy} \sim 150$ S/cm and magnetooptical response on the level of $\varepsilon_{xy}(\omega) \sim \pm 10$. We will show that the AK mechanism ensures large Berry curvature on the Fermi surfaces. This AK mechanism is very robust, in sharp contrast with the conventional mechanisms operative in ferromagnets, which rely on fine tuning of nodal lines or Weyl points close to the Fermi level (23–25). Since CrSb$_2$−FeSb$_2$ − CoSb$_2$ forms a continuous solid solution with a marcasite (pseudo-marcasite for high Co content) structure (21, 22), such doping should be accessible experimentally, and thus, this system represents a prime candidate for testing the predicted anomalous responses.
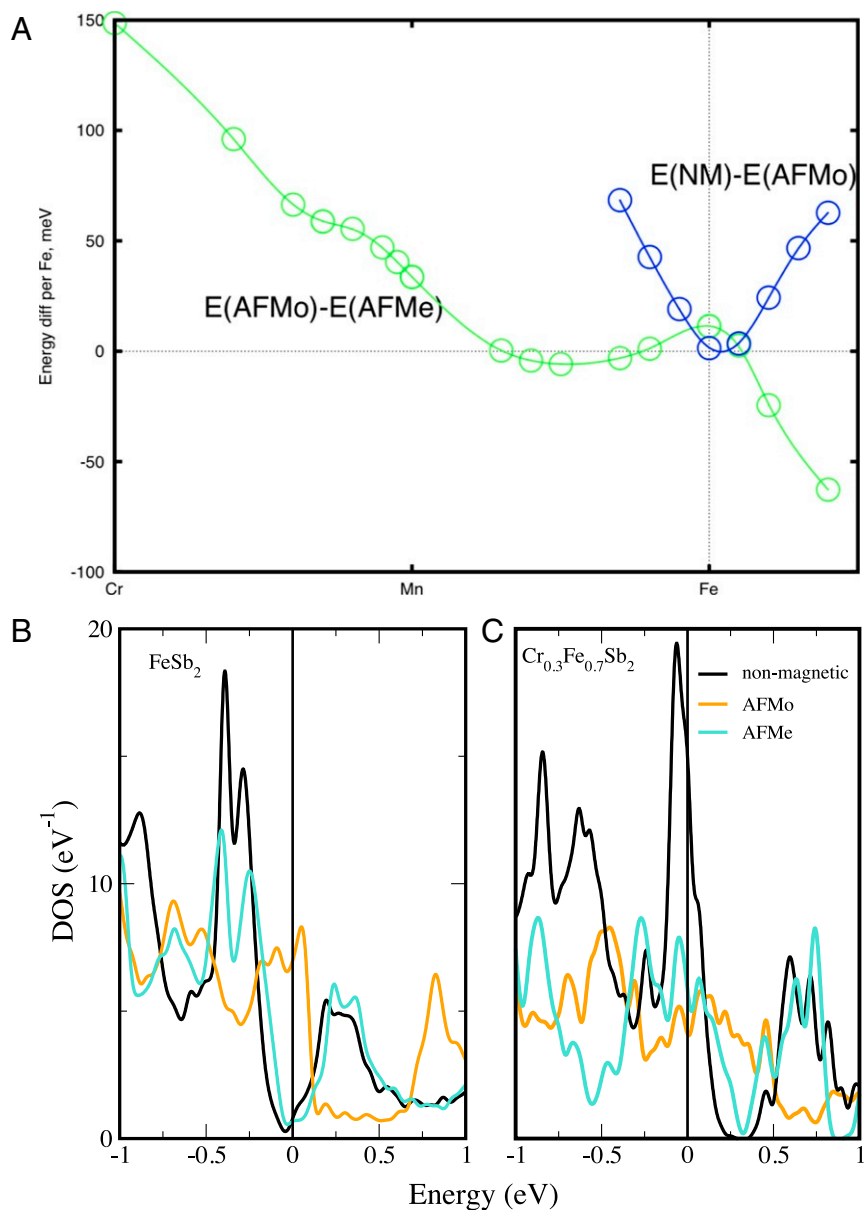
Antiferromagnetic Ground States in FeSb$_2$

The marcasite crystal structure of FeSb$_2$ exhibits the nonmagnetic orthorhombic symmetry space group $Pnnm$. Previous first principles studies assumed that Fe electrons are strongly correlated, resulting in a competitive metaferromagnetic state with Fe magnetization on the order of 1 μ_B (26). However, these calculations did not address the possibility of antiferromagnetic order in FeSb$_2$, although antiferromagnetism has been studied in another marcasite crystal, CrSb$_2$ (27).

In our calculations, we consider the two antiferromagnetic orderings shown in Fig. 1 A and B. The former, known in the literature as AFMe (27), is an ordinary Kramers AF (KAF). It is obtained by doubling the nonmagnetic unit cell along the [011] direction. The latter ordering (Fig. 1B), known as AFMo (27), preserves the size of the nonmagnetic unit cell and is an AK magnet, wherein the spin polarization is nonzero and changes sign both in real (from one Fe to the other) and in reciprocal (across the nodal planes, shown in Fig. 1D) space.

In Fig. 2A, we show our calculated ground-state energy differences as a function of doping on the Fe site. We employed both the virtual crystal approximation (VCA) and supercell first principles calculations (*Methods*). First, we focus on electron and hole doping around the Fe stoichiometric point corresponding to the blue curve in Fig. 2A. The KAF is lower in energy than the nonmagnetic state (blue curve) in this region except in the vicinity of the stoichiometric Fe point, where it is only marginally (~ 1 meV/Fe) more stable. Enhancing the tendency to magnetism by adding a Hubbard U (LDA+U) obviously stabilizes the KAF magnetic solution even further. However, given the

Fig. 2. (*A*) A plot of the total energy of FeSb$_2$ with different imposed magnetic orderings as a function of hole and electron doping in the VCA approximation. (*B* and *C*) Density of states (DOS) for FeSb$_2$ and Co$_{0.3}$Fe$_{0.7}$Sb$_2$ in the VCA, illustrating the removal of weight from E$_F$ upon hole doping in the AFMo and FM patterns but an increase in weight for the nonmagnetic state. The KA gains some weight at E$_F$.

experimental situation, LDA+U may, in fact, be less accurate than standard DFT (*Methods* discusses the choice of the density functional used).

Next, we discuss the energetics of the two antiferromagnetic phases (green curve in Fig. 2*A*). For stoichiometric Fe, Cr, and MnSb$_2$, the KAF state is lower than the AK one by ≈ 11 meV or ≈ 120 K per Fe (Fig. 2*A*) for pure FeSb$_2$. The lower energy of the KAF structure can be related to opening a pseudogap in the density of states, nearly identical to the nonmagnetic pseudogap. The spin-split AK phase, on the other hand, is a good metal, with the corresponding loss of the one-electron energy. There are two corollaries of this finding. First, the near degeneracy of two rather different magnetic states, commonly seen in frustrated magnetic systems, is liable to both suppress ordered states and stabilize the dynamically nonmagnetic one. Second, one can conjecture that if the material is doped in either direction and the disadvantage of the spin-split

antiferromagnetic phase is alleviated, the latter will become the most stable.

Strong fluctuations stemming from these competitions may play an important role in the thermoelectricity of FeSb$_2$, through an energy dependence of the scattering rate. As discussed in the review by Tomczak (28), the thermoelectric power (TEP) of FeSb$_2$ greatly exceeds the theoretical limit for a purely electronic system, and it is necessary to account for a secondary bosonic subsystem contributing to TEP via boson drag. At the same time, this review points out that the standard phonon drag cannot explain the TEP in FeSb$_2$ and suggests the possibility of in-gap states interacting with the phonons. While this remains a possible scenario, our calculations suggest the presence of strong antiferromagnetic fluctuations as an alternative bosonic system. Whether these excitations may be successful in explaining the TEP in FeSb$_2$ remains to be seen, and a thorough analysis is beyond the scope of this paper.

Mazin et al.
Prediction of unconventional magnetism in doped FeSb$_2$

PNAS | 3 of 8
https://doi.org/10.1073/pnas.2108924118

As expected, our VCA calculations predict that moderate electron or hole doping does stabilize the spin-split antiferromagnetic order. To illustrate the role of the pseudogap, we compare the FeSb$_2$ density of states with that for the electron-doped Co$_{0.3}$Fe$_{0.7}$Sb$_2$ in Fig. 2C. The spin-split antiferromagnetic ordering has the highest weight at the Fermi energy in the former case and the lowest in the latter case. Total energy calculations in Fig. 2A confirm that in the calculations, the AFMo structure is the most stable in the same range of either electron or hole doping. The energy gain due to the antiferromagnetism with respect to the nonmagnetic phase grows extremely rapidly with doping, suggesting that, except in close vicinity to the stoichiometric compound, the competition is between different magnetic phases.

Nonrelativistic Symmetry Analysis of AK Spin Splitting

We now consider the symmetries of the magnetic phases. The spin degeneracy in the FeSb$_2$ collinear KAF phase is due to the combined $t\mathcal{T}$ symmetry (the former is a partial unit cell translation, and the latter is time reversal). Alternatively, one can say that it is protected by the combined (as opposed to individual) $\mathcal{PT}$ symmetry (29). The antiferromagnetism is constructed by doubling the unit cell, along the [011] direction. The opposite magnetic sublattices in the KAF phase are thus connected by the nonmagnetic unit cell translations combined with time reversal.

In the unconventional AK phase, magnetic order does not change the size of the unit cell, and the crystal lacks both $t\mathcal{T}$ and $\mathcal{PT}$ symmetries and thus allows for spin splitting at a general wave vector.

If we neglect the spin–orbit interaction, the real space and the spin space are decoupled. The resulting nonrelativistic symmetry space group (8, 30) of FeSb$_2$ includes the following symmetry operations:

$$\{\mathcal{E}, \mathcal{P}, \mathcal{M}_z, \mathcal{C}_{2z}\} + t'\mathcal{R}_S\{\mathcal{C}_{2x}, \mathcal{M}_x, \mathcal{C}_{2y}, \mathcal{M}_y\}. \qquad [2]$$

Here, $\mathcal{R}_S$ changes the sign of the spin quantization axis and is therefore the nonrelativistic analog of time reversal. The remaining operations $\mathcal{P}$, $\mathcal{M}$, and $\mathcal{C}_2$ are unitary symmetries acting in the real space, and these symmetries map each magnetic sublattice onto itself. In contrast, the remaining four symmetries include $\mathcal{R}_S$ and map the two opposite magnetic sublattices onto each other, combined with the half-unit cell translation $t' = \left(\frac{1}{2}\frac{1}{2}\frac{1}{2}\right)$. This reflects the fact that in the nonmagnetic $Pnnm$ group, $\mathcal{P}$, $\mathcal{M}_z$, and $\mathcal{C}_{2z}$ are symmorphic operations, while the rest are glide planes and screw axes.

We can understand the AK band structure by analyzing the action of symmetries in the momentum space. Here, we demonstrate the action of $\mathcal{R}_S\mathcal{M}_x$:

$$\mathcal{R}_S\mathcal{M}_x E(k_x, k_y, k_z, \sigma) = E(-k_x, k_y, k_z, -\sigma). \qquad [3]$$

Thus, $E(k_x, k_y, k_z, \uparrow) = E(-k_x, k_y, k_z, \downarrow)$, and for $k_x = 0$, the two spins are degenerate, $E(0, k_y, k_z, \uparrow) = E(0, k_y, k_z, \downarrow)$. On the other hand, both spin-up and spin-down bands must separately respect the Bloch theorem, so $E(\mathbf{k}, \uparrow) = E(\mathbf{k} - \mathbf{G}, \downarrow)$. Using $\mathbf{G} = (2\pi, 0, 0)$, we see that $E(-\pi, k_y, k_z, \uparrow) = E(\pi, k_y, k_z, \uparrow) = E(-\pi, k_y, k_z, \downarrow)$. This set of rules (similarly for k_y) generates the set of nodal planes shown in Fig. 1 and the functional form of Eq. 1. Note that while the location of such nodal surfaces depends on the exact nature of the operations in the second term in Eq. 2, their presence is a universal feature of AK magnets [cf., e.g., previously discussed tetragonal RuO$_2$ (1), MnO$_2$ (5), and MnF$_2$ (4)].

Away from the nodal planes, the absolute value of the spin splitting obeys the full nonmagnetic crystal symmetry, while its sign alternates (8, 30), ensuring that the material as a whole is spin compensated by symmetry. As an illustration of this, Fig. 3
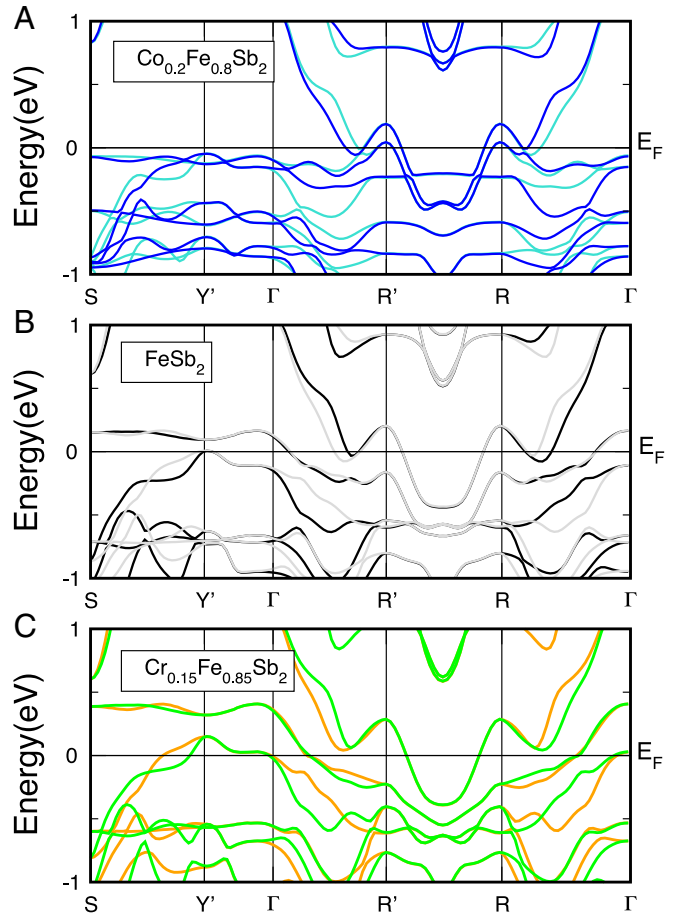

Fig. 3. The nonrelativistic band structure of FeSb$_2$ with the AK pattern for (A) electron doped, (B) stoichiometric, and (C) hole doped and corresponding Fermi surfaces. The up and down bands split along low symmetric momenta in accordance with *SI Appendix*, Tables S1 and S2. Furthermore, the splitting exactly reverses along perpendicular momenta (i.e., ΓR and $\Gamma R'$). This explains the overall net zero moment.

shows bands along the path $\Gamma RR'\Gamma$ as shown in Fig. 1D. The full spin splitting and nodal structure can be seen in the Fermiology throughout the BZ shown in Fig. 1D and in *SI Appendix* for all dopings. In *SI Appendix*, we also list the degeneracies along the high-symmetry lines and planes in the BZ (*SI Appendix*, Tables S1 and S2).

We emphasize the distinction between spin splitting by antiferromagnetism and by relativistic interactions. The spin–orbit spin splitting (e.g., Rashba or Ising in two dimensions) is characterized by spin-degenerate points at the time-reversal symmetry invariant momenta protected by the time-reversal symmetry. Away from these points, the bands spin split antisymmetrically:

$$E(\mathbf{k}, \uparrow) = E(-\mathbf{k}, \downarrow) \qquad [4]$$

[i.e., the spin splitting $E(\mathbf{k}, \uparrow) = E(-\mathbf{k}, \downarrow)$ follows a $p-$ or $f-$wave symmetry rather than d wave, as in Eq. 1]. This is related to the fact that spin orbit splitting can only happen in noncentrosymmetric crystals, whereas in the absence of spin–orbit, the $E(\mathbf{k}, \sigma) = E(-\mathbf{k}, \sigma)$ holds independent of the magnetic structure (the time-reversal symmetry can be applied to the Schrödinger equation for each spin separately).

Relativistic Symmetry Analysis and Electronic Structure

From the experimental point of view, the most important prediction is that the easy magnetization axis for FeSb$_2$ is

calculated to be [010] (Table 1). Indeed, as mentioned in the introduction, unconventional antiferromagnetism with alternating spin splitting is, in principle, not that rare, but those few cases so far identified as metals do not necessarily have the magnetization direction conducive to anomalous transport (as discussed with respect to RuO_2 in ref. 1). In $FeSb_2$, to be specific, two out of three orthorhombic directions manifest the latter ([100] and [010]), and the third does not (Table 1; *SI Appendix*, Tables S1 and S2 show the spin–orbit-induced splittings). Fortunately, Cr (but not Co) doping not only preserves the favorable magnetic anisotropy but even enhances it. In Fig. 4*A*, we show the calculated magnetization density isosurfaces for the magnetization along the [010] direction (calculated in Vienna Ab-initio Simulation Package [VASP]) (*Methods*). The anisotropic spin densities highlight the breaking of the $t\mathcal{T}$ and $\mathcal{PT}$ symmetries.

In the following, we illustrate how the symmetry analysis of the spin splitting proceeds in the relativistic case. In this case, we need to take into account the full magnetic space group (MSG), which depends on the selected spin quantization axis; for instance, a mirror plane $\mathcal{M}_y$ conserves the spin components s_y but flips the directions of s_x and s_z. For the spin direction along the easy axis [010] direction, the MSG is $Pnn'm'$ (i.e., the glide and the mirror planes symmetries for the y and z planes, respectively, are preserved only when combined with the time-reversal symmetry) and includes the following symmetry operations ($t' = [\frac{1}{2}\frac{1}{2}\frac{1}{2}]$):

$$\{\mathcal{E}, \mathcal{P}\} + t'\{\mathcal{C}_{2x}, \mathcal{M}_x\} + \mathcal{T}\{\mathcal{C}_{2z}, \mathcal{M}_z\} + t'\mathcal{T}\{\mathcal{C}_{2y}, \mathcal{M}_y\}. \quad [5]$$

The notations are the same as in Eq. **2**, but the spatial and spin-space symmetries are now coupled, resulting in a different structure of the symmetry group and band degeneracies. We also note that the $Pnn'm'$ is type III MSG and thus describes an AF with the nonmagnetic unit cell preserved.

In Fig. 4*B*, we show the calculated relativistic energy bands with spins along the [010] direction and including spin–orbit. By comparing these bands with the nonrelativistic ones, we confirm the collinear antiferromagnetism as the main source of the spin splitting in $FeSb_2$. The spin–orbit interaction additionally splits certain high-symmetry planes, lines, and points as summarized in *SI Appendix*, Tables S1 and S2. However, the relativistic spin splitting is much weaker.

Not all nodal planes shown in Fig. 1*D* are preserved, but one plane, $k_y = \pm\pi$, is, as we explain below. Let us denote $\{t'|\mathcal{T}\mathcal{C}_{2y}\} = \mathcal{T}\mathcal{S}_{2y}$. The space operation alone, $\mathcal{S}_{2y}$, translates the first Fe, Fe1, into its AF counterpart Fe2. If the spin of Fe1 (2) is $s_y(-s_y)$, $\mathcal{S}_{2y}$ alone is not a symmetry operation, but $\mathcal{T}\mathcal{S}_{2y}$ is. Conversely, for the spin $s_x(-s_x)$, $\mathcal{S}_{2y}$ is a symmetry operation but not $\mathcal{T}\mathcal{S}_{2y}$. The same is true for s_z. This is why for spins along x, y, or z, the MSG is $Pn'nm'$, $Pnn'm'$, or $Pnnm$, respectively.

We will now demonstrate the symmetry protection of nodal surfaces. We consider two Bloch functions, $\varphi_\mathbf{k}$ and

Table 1. The Hall conductivity in Siemens per centimeter and the easy axis with magnetic anisotropy energy (MAE) in millielectronvolts relative to the next favorable axis ([001])

	$FeSb_2$	$Cr_{0.15}Fe_{0.85}Sb_2$	$Co_{0.2}Fe_{0.8}Sb_2$
σ_{yz}	143	−31	94
Next favorable axis	[001]	[001]	[010]
Easy axis	[010]	[010]	[001]
MAE	−0.12	−0.25	−0.12

$\varphi'_\mathbf{k}$, related by the nonsymmorphic symmetry operation $\mathcal{O} = \mathcal{T}\mathcal{S}_{2y}$:

$$E_{\mathbf{k}'}\varphi'_{\mathbf{k}'}(\mathbf{r}) = H(\mathbf{r})\varphi'_{\mathbf{k}'}(\mathbf{r}) = H(\mathbf{r})[\mathcal{O}\varphi_\mathbf{k}(\mathbf{r})] \quad [6]$$
$$\mathcal{O}[H(\mathbf{r})\varphi_\mathbf{k}(\mathbf{r})] = E_\mathbf{k}[\mathcal{O}\varphi_\mathbf{k}(\mathbf{r})]. \quad [7]$$

Here, we should remember that $\mathbf{k}' = \mathcal{O}\mathbf{k} \neq \mathbf{k}$, and we should remember that $\mathcal{O}$ is a symmetry operation of the Hamiltonian, $\mathcal{O}H(\mathbf{r})\mathcal{O}^{-1} = H(\mathbf{r})$. We see that the energies $E_\mathbf{k}$ and $E_{\mathbf{k}'}$ of the two Bloch states, $\varphi_\mathbf{k}(\mathbf{r})$ and $\varphi'_{\mathbf{k}'}(\mathbf{r})$, are identical. That means that either $\varphi_\mathbf{k}(\mathbf{r})$ and $\varphi'_{\mathbf{k}'}(\mathbf{r})$ are identical or these are two genuinely degenerate states. In order to demonstrate the latter, we calculate the overlap of the two functions:

$$\langle\varphi'_{\mathbf{k}'}(\mathbf{r})|\varphi_\mathbf{k}(\mathbf{r})\rangle = \langle\mathcal{O}\varphi'_{\mathbf{k}'}(\mathbf{r})|\mathcal{O}\varphi_\mathbf{k}(\mathbf{r})\rangle = \mathcal{O}^2\langle\varphi_\mathbf{k}(\mathbf{r})|\varphi'_{\mathbf{k}'}(\mathbf{r})\rangle. \quad [8]$$

Now, by definition, $\mathcal{O}^2 = t'\mathcal{T}\mathcal{C}_{2y}t'\mathcal{T}\mathcal{C}_{2y} = e^{i(-k_x+k_y-k_z)/2}e^{i(k_x+k_y+k_z)/2} = e^{ik_y}$ so $\langle\varphi_\mathbf{k}(\mathbf{r})|\varphi'_{\mathbf{k}'}(\mathbf{r})\rangle = e^{ik_y}\langle\varphi_\mathbf{k}(\mathbf{r})|\varphi'_{\mathbf{k}'}(\mathbf{r})\rangle$: that is to say, $\varphi_\mathbf{k}(\mathbf{r})$ and $\varphi'_{\mathbf{k}'}(\mathbf{r})$ are not identical and moreover, are orthogonal, unless $k_y = 0$. Next, we note that two vectors, $k_y = \pi$ and $k'_y = -\pi$, are related by the operation $\mathcal{O} = \mathcal{T}\mathcal{S}_{2y}$ and at the same time, by the reciprocal lattice vector $G = 2\pi$. This proves that at the plane $k_y = \pi$, there are two orthogonal wave functions giving the same electron energy, even with spin–orbit, if the sublattice magnetization direction is y. Obviously, the same proof applies to $k_x = \pi$ and the sublattice magnetization direction x.

We note that our protecting antiunitary screw symmetry is oriented along the antiferromagnetic sublattices, and its orientation can be controlled by the magnetic quantization axis (along the x or y direction). This contrasts with the ferromagnetic nodal surfaces protected by the antiunitary screw axis present for magnetization perpendicular to the symmetry axis (31).

In Fig. 4*D*, we show the spin polarization at the Fermi surface. We observe that most of the Fermi sheets are spin polarized, but near the former nodal planes $k_{x,y} = 0$, the spin direction continuously rotates from one direction to the opposite. This feature makes the $FeSb_2$ antiferromagnet a promising spin current generator (10).

Note that for the spins along the [001] crystal axis, when the MSG is $Pnnm$, the three mirror symmetries prohibit the existence of a ferromagnetic pseudovector and thus, spontaneous Hall conductivity (1). For spins along [100], the MSG allows a nonzero anomalous Hall conductivity and magnetooptical (nondiagonal) components of the dielectric function, which are σ_{xz} (σ_{yz}) for $Pn'nm'$ ($Pnn'm'$).

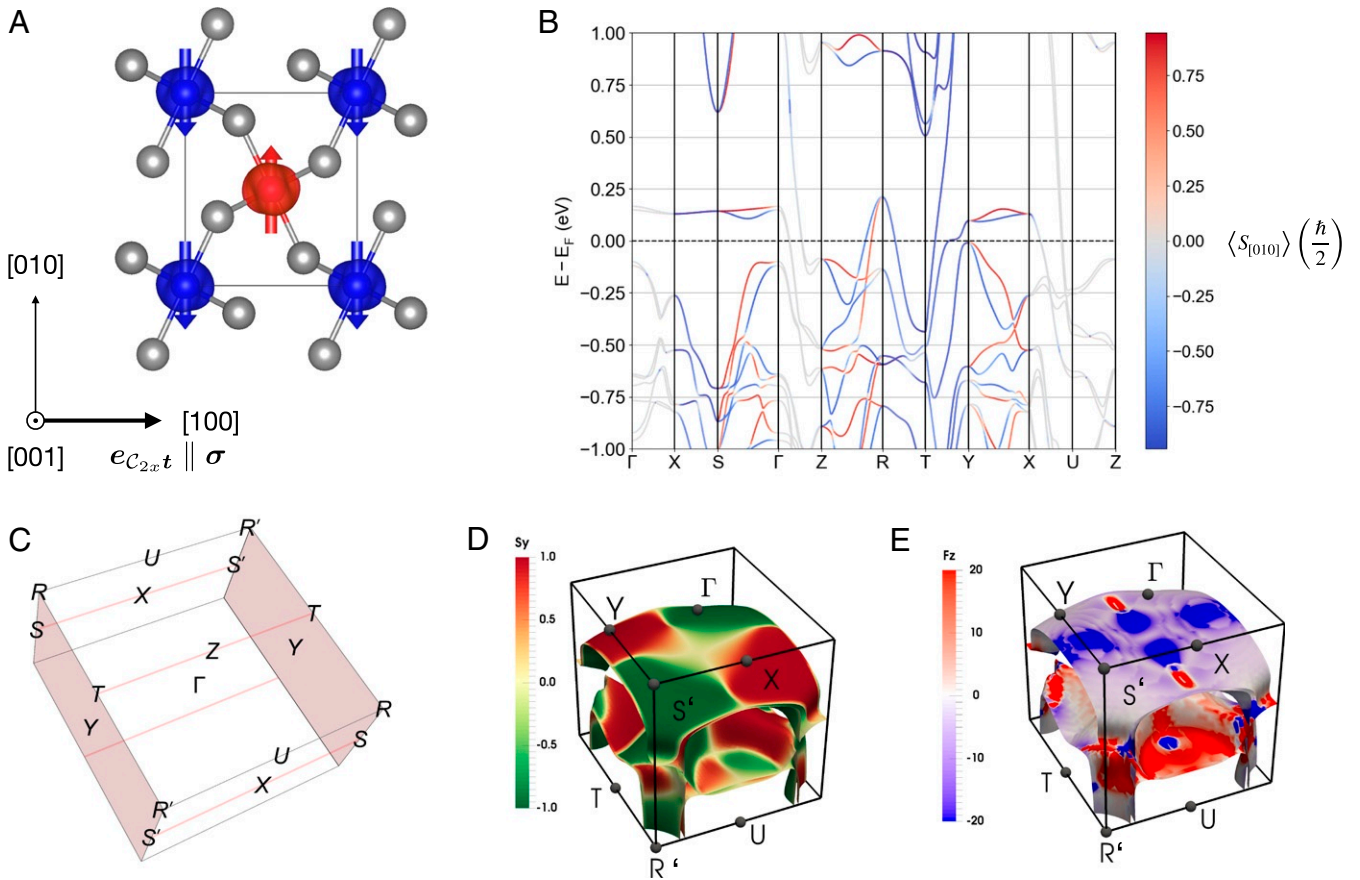## Anomalous Electric and Magnetooptical Response

We shall now discuss the nontrivial ramifications of the momentum space-dependent splitting and the presence of AK nodal surfaces, which manifest themselves in the anomalous Hall effect and other response functions.

Berry Curvature. We start by discussing the Berry curvature calculations shown in Fig. 4*E* and *SI Appendix*, Fig. S2. We observe that the large Berry curvature originates from the regions of the BZ that are degenerate without spin–orbit interaction. The presence of the spin–orbit interaction splits these nodal features and generates anisotropic Berry curvature as we show in Fig. 4*E*, including the former nodal planes. The fact that the AKAF nodal manifolds are surfaces, and not lines, ensures a large Berry curvature contribution from regions in the BZ where the nodal surface intersects the mirror planes.

Crystal Hall Effect. The Hall vector direction follows simple rules (1). The Hall vector $\boldsymbol{\sigma}$ is parallel to the rotational axis of

Mazin et al.
Prediction of unconventional magnetism in doped $FeSb_2$

PNAS | 5 of 8
https://doi.org/10.1073/pnas.2108924118

Fig. 4. Electronic structure of FeSb$_2$ with spin–orbit interaction. (*A*) Unit cell with the calculated magnetization densities; marked symmetry group generators $\mathcal{P}$, $\mathcal{C}_{2a}t$, and $\mathcal{C}_{2z}\mathcal{T}$; and Hall vector σ. (*B*) Spin-projected energy bands calculated with the spin–orbit interaction and sublattice magnetization along the [010] crystal direction. The bands with overlapping blue and red are spin-degenerate, and grey-shaded ones are spin split by spin–orbit but still not spin polarized along the antiferromagnetic vector. (*C*) BZ band degeneracy manifolds in the presence of the spin–orbit interaction are marked by red shading. (*D*) Spin-projected Fermi surfaces along the [010] quantization axis. (*E*) Berry curvature resolved on the Fermi surface reveals large contributions from gapped AK nodal features at $k_{x,y} = 0$ planes marked by high-intensity blue and red color.

$\mathcal{C}_{2x}t'$ symmetry as shown in Fig. 4*A*. The amplitude of the intrinsic spontaneous Hall effect can be calculated by integrating the Berry curvature over the BZ. We see in Fig. 5*A* that while the Berry curvature changes sign, the cancellation is incomplete, and the Hall conductivity σ_{yz} is nonzero; σ_{xy} and σ_{xz} vanish, in agreement with our symmetry analysis (1). We show the resulting energy dependence of the Hall conductivity in Fig. 5*A* for the three doping levels discussed in *Nonrelativistic Symmetry Analysis of AK Spin Splitting* (*SI Appendix*, Fig. S3).

At the Fermi level, we obtain, for the [010] spin direction, 143 S/cm for the undoped compound and 94 and −31 S/cm for the Co- and Cr-doped compounds, respectively. Note, however, that the calculated easy axis in the Co-doped compound is [001], which does not afford an anomalous response. We conclude that the Cr-doped FeSb$_2$ is the best candidate for the experimental observation of the spontaneous crystal Hall effect. Previously, the crystal Hall effect was experimentally observed in RuO$_2$ but only after a spin-reorientation transition, induced by a strong external magnetic field (7).

Crystal Magnetooptical Kerr Effect. The magnetooptical Kerr effect is a dynamic counterpart of the direct-current anomalous Hall effect and follows the analogous symmetry-determined selection rules. It is the method of choice for checking for ferro- and ferrimagnetic transitions and is routinely used as a litmus test for nonzero net magnetization and/or non-

collinear antiferromagnetism (32–35). In accordance with that, the easy axis that affords a sizable Hall conductivity also suggests, contrary to the common wisdom, the presence of magnetooptical effects in this fully compensated collinear material.

The complex Kerr rotation angle is proportional, in this case, to the yz component of the complex dielectric function, $\varepsilon_{yz}(\omega)$. The proportionality coefficient depends on the diagonal (Drude) dielectric function and thus, on the sample-dependent relaxation rate. For that reason, we present in Fig. 5*B* only the corresponding nondiagonal components of the interband dielectric function, $\mathrm{Re}\,\varepsilon_{ij}(\omega)$ and $\mathrm{Im}\,\varepsilon_{ij}(\omega)$ calculated from first principles (*Methods*). Note that the $\omega \to 0$ limit of the intraband conductivity tensor, $\sigma_{ij}(\omega) = \frac{\omega}{4\pi}\mathrm{Im}\,\varepsilon_{ij}(\omega)$, is the anomalous Hall conductivity (32). In agreement with the symmetry analysis and the Hall effect calculations, we find for the spin along [010] ([100]) a nonzero $\varepsilon_{yz}(\omega)$ [$\varepsilon_{xz}(\omega)$]. We obtain the largest magnitude for $\sigma_{yz}(\omega)$ at $\omega \approx 0.8$ eV, which is approximately five times larger than the dc Hall conductivity. The magnitude of the magnetooptical effects in FeSb$_2$ is comparable with that in typical ferromagnets.

Discussion

Recently, a general group theory of unconventional antiferromagnetism with nonrelativistic alternating spin splitting in momentum space was developed (30). According to this theory, doped FeSb$_2$ belongs to the unconventional collinear
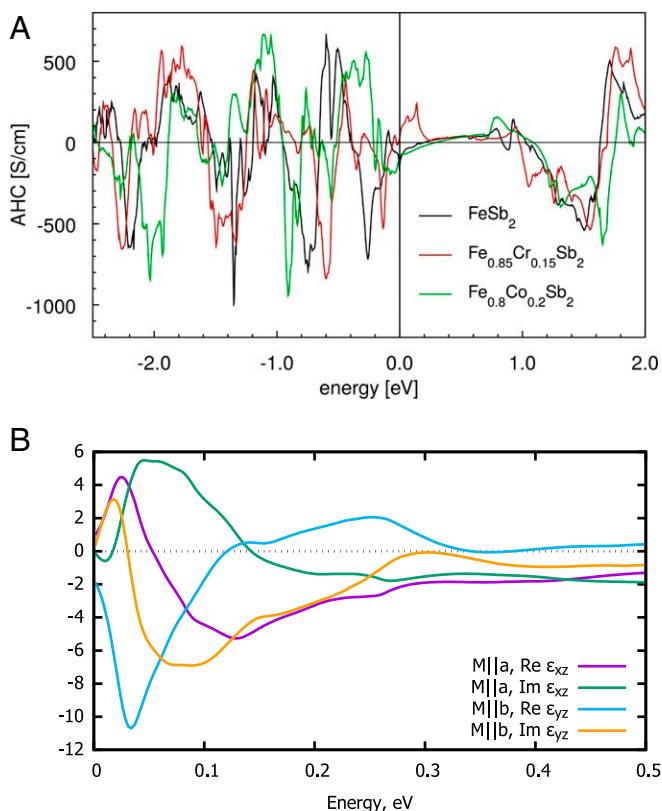
Fig. 5. Anomalous charge and optical response. (*A*) Energy dependence of the anomalous Hall conductivity (AHC) on the energy for the stoichiometric $FeSb_2$ and electron- and hole-doped variants. (*B*) Energy (frequency) dependence of the off-diagonal optical conductivity tensor calculated in stoichiometric $FeSb_2$, which determines the magnetooptical Kerr effect (9).

magnetic phase with the alternating spin–momentum–texture winding number two and represents an experimentally attractive material platform for novel nonrelativistic and relativistic spintronics effects (1, 10, 12, 36), which we now discuss.

The unconventional antiferromagnetic phase of doped $FeSb_2$ should exhibit a nonrelativistic electric spin-splitter effect (10). For instance, the application of an electric current along the [110] direction will generate a longitudinal spin-polarized current that can be directly measured or furthermore, can be employed for building a giant magnetoresistance device (12). In our paper, we have calculated a strong Hall conductivity that originates from symmetry breaking due to the tilted Sb octahedra, a mechanism referred to as the crystal Hall effect (1, 9, 37). Importantly, we have predicted the easy axis compatible with the crystal Hall current in a metallic AF, a highly sought-after property, which has been elusive so far (36). The crystal Hall effect could be thus straightforwardly measured. One could grow single crystals or epitaxially grow monocrystalline thin films of [100]-oriented $Cr_{0.15}Fe_{0.85}Sb_2$. Applying an electric field along the [001] axis should generate a large Hall voltage along the [010] direction, measurable by sweeps in the magnetic field oriented out of plane.

Theoretically, we have demonstrated a large contribution to the crystal Hall conductivity from the AK nodal surfaces. The AK nodal surfaces are pseudonodal surfaces, which we have shown are partly gapped by the spin–orbit interaction and generate large anomalous Berry curvature. The AK nodal surfaces are enforced by antiferromagnetic symmetries ensuring their presence for arbitrary filling. This symmetry enforcement is not available in ferromagnets with accidental pseudonodal lines such that

they have to be fine tuned to the Fermi level (23–25). Finally, the nodal surface spin–orbit gap can be manipulated by reorienting the antiferromagnetic vector. This sensitivity can lead to interesting functionalities, e.g., large anisotropic magnetoresistance effects analogous to effects predicted in the CuMnAs AF (29). Our results thus prompt further research in magnetotransport effects in this recently discovered class of magnets.

Summary

We have discussed the recently discovered phenomenon in which collinear antiferromagnetic order results in nondegenerate energy bands that give rise to magnetic properties characteristic of both AFs and ferromagnets. With a particular magnetic anisotropy, these materials also display various anomalous properties. As a platform to illustrate computational design of potentially novel magnetic materials with alternating spin-momentum locking, we calculate the electronic properties of the famous thermoelectric, $FeSb_2$. We demonstrate that, other than the experimentally observed narrow-gap nonmagnetic semiconductor ground state, there are two nearly degenerate magnetic states, one a conventional AF and the other an AF with alternating spin splitting (but not a ferromagnet, as proposed earlier). Our first principles calculations suggest that the unconventional antiferromagnetic state can be stabilized in a narrow range of electron or hole doping. We further investigate the magnetic properties of thus stabilized $FeSb_2$, laying out a systematic protocol, which includes as successive steps a nonrelativistic symmetry analysis, nonrelativistic band structure calculations, a relativistic symmetry analysis, relativistic calculations of magnetic anisotropy, and finally, relativistic calculations of the band structure and signature properties, such as anomalous Berry curvature from AK nodal surfaces, the crystal Hall effect, and the crystal magnetooptical Kerr effect. We have also described feasible experimental geometries for observation of these effects. We hope that this work will pave the way for computational prediction and analysis of a broad spectrum of AFs with nonrelativistic alternating spin-momentum coupling (30) that showcase these recently discovered phenomena.

Methods

We used the VASP (38) with the Perdew–Burke–Ernzerhof (PBE)-generalized gradient approximation (GGA) approximation to the exchange correlation potential (39) and projector augmented wave pseudopotentials (40) to fully relax $FeSb_2$ in a variety of magnetic patterns. We found that not only was the AFMe pattern the lowest in energy, but the resulting lattice parameters of $a = 5.8379$, $b = 6.5248$, and $c = 3.1811$ matched extremely well with the measured parameters of $a = 5.8328$, $b = 6.53758$, and $c = 3.19730$ (41).

To verify the energy orderings of the different magnetic orderings with the highest possible accuracy, we calculated each one with the full potential local orbital (FPLO) code (42) and also with the PBE-GGA approximation but adding spin–orbit coupling via a fully relativistic four-component solution to the Dirac equation. We found that the energy differences shifted by less than 0.2 meV due to the inclusion of this term. To simulate doping, we used the Wien2k code (43) (again with PBE-GGA) and employed the VCA with the structure held constant according to the measurements in ref. 41. This shifts the charge of the ion cores to an average of the two charged species being simulated. This method allows electrons/holes to be added to the system in an average band-like manner, consistent with experimental measurements that find a lack of local moments in favor of a fluctuating itinerant magnetic state (44, 45).

In our VASP calculations of the band structure and magnetization densities in Fig. 4, we set the energy cutoff to 520 eV and use the momentum mesh of $7 \times 6 \times 12$, and we use the GGA potential with the Vosko–Wilk–Nusair potential. For plotting the spin-polarized energy bands in Fig. 4, we used the PyProcar script (46). Furthermore, we use the Wannier90 code (47) to construct the Wannier functions (WFs). We calculate the spontaneous Hall conductivity by integrating the Berry curvature in the BZ in the WannierTools code (48). To corroborate the results for the Hall conductivity and to extend them to the doped cases $Cr_{0.15}Fe_{0.85}Sb_2$ and $Co_{0.2}Fe_{0.8}Sb_2$ via VCA, we repeated the calculation using maximally projected WFs (49) as provided by FPLO (version 19.00) in full relativistic

mode with subsequent integration of the Berry curvature. We projected onto a set of Fe $3d$ and Sb $5p$ orbitals, which generates WFs for all bands in $[-6, 6]$ eV with only tiny Wannier fit errors of about 3 meV. The Berry curvature was calculated by the method of ref. 50 using only the dominant term (which was checked to be a rather small error). The integration of the Berry curvature using the Wannier model was performed with a k mesh of $301 \times 301 \times 602$ and $400 \times 400 \times 800$ points for the undoped and doped compounds, respectively. The convergence was better than 5% error for the Hall conductivity at the Fermi level. Calculations of the optical response were performed with the Wien2k code (43).

1. L. Šmejkal, R. González-Hernandez, T. Jungwirth, J. Sinova, Crystal hall effect in collinear antiferromagnets. *Sci. Adv.* **6**, eaaz8809 (2020).
2. K. H. Ahn, A. Hariki, K. W. Lee, J. Kuneš, Antiferromagnetism in RuO2 as d-wave Pomeranchuk instability. *Phys. Rev. B* **99**, 184432 (2019).
3. S. Hayami, Y. Yanagi, H. Kusunose, Momentum-dependent spin splitting by collinear antiferromagnetic ordering. *J. Phys. Soc. Jpn.* **88**, 123702 (2019).
4. L. D. Yuan, Z. Wang, J. W. Luo, E. Rashba, A. Zunger, Giant momentum-dependent spin splitting in centrosymmetric low z antiferromagnets. *Phys. Rev. B* **102**, 014422 (2020).
5. Y. Noda, K. Ohno, S. Nakamura, Momentum-dependent band spin splitting in semiconducting MnO2: A density functional calculation. *Phys. Chem. Chem. Phys.* **18**, 13294–13303 (2016).
6. S. López-Moreno, A. H. Romero, J. Mejía-López, A. Muñoz, I. V. Roshchin, First-principles study of electronic, vibrational, elastic, and magnetic properties of FeF{}_{2} as a function of pressure. *Phys. Rev. B Condens. Matter Mater. Phys.* **85**, 134110 (2012).
7. Z. Feng *et al.*, Observation of the crystal Hall effect in a collinear antiferromagnet. arXiv [Preprint] (2020). https://arxiv.org/abs/2002.08712 (Accessed 24 September 2021).
8. H. Reichlová *et al.*, Macroscopic time reversal symmetry breaking arising from antiferromagnetic Zeeman effect. arXiv [Preprint] (2020). https://arxiv.org/abs/2012.15651 (Accessed 24 September 2021).
9. K. Samanta *et al.*, Crystal Hall and crystal magneto-optical effect in thin films of SrRuO{}_{3}. *J. Appl. Phys.* **127**, 213904 (2020).
10. R. González-Hernández *et al.*, Efficient electrical spin splitter based on nonrelativistic collinear antiferromagnetism. *Phys. Rev. Lett.* **126**, 127701 (2021).
11. M. Naka, Y. Motome, H. Seo, Perovskite as a spin current generator. *Phys. Rev. B* **103**, 125114 (2021).
12. L. Šmejkal, A. B. Hellenes, R. González-Hernández, J. Sinova, T. Jungwirth, Giant and tunneling magnetoresistance effects from anisotropic and valley-dependent spin-momentum interactions in antiferromagnets. arXiv [Preprint] (2021). https://arxiv.org/abs/2103.12664 (Accessed 24 September 2021).
13. D.-F. Shao, S.-H. Zhang, M. Li, E. Y. Tsymbal, Spin-neutral currents for spintronics. arXiv [Preprint] (2021). https://arxiv.org/abs/2103.09219 (Accessed 24 September 2021).
14. C. Homes *et al.*, Unusual electronic and vibrational properties in the colossal thermopower material FeSb2. *Sci. Rep.* **8**, 11692 (2018).
15. A. Herzog *et al.*, Strong electron correlations in FeSb2: An optical investigation and comparison with RuSb2. *Phys. Rev. B Condens. Matter Mater. Phys.* **82**, 245205 (2010).
16. P. Sun, N. Oeschler, S. Johnsen, B. B. Iversen, F. Steglich, Narrow band gap and enhanced thermoelectricity in FeSb2. *Dalton Trans.* **39**, 1012 (2010).
17. C. J. Kang, G. Kotliar, Study for material analogs of FeSb2: Material design for thermoelectric materials. *Phys. Rev. Mater.* **2**, 034604 (2018).
18. J. Tomczak, K. Haule, T. Miyake, A. Georges, G. Kotliar, Thermopower of correlated semiconductors: Application to FeAs2 and FeSb2. *Phys. Rev. B Condens. Matter Mater. Phys.* **82**, 085104 (2010).
19. A. Bentien, G. Madsen, S. Johnsen, B. Iversen, Experimental and theoretical investigations of strongly correlated FeSb2−xSnx. *Phys. Rev. B Condens. Matter Mater. Phys.* **74**, 25105 (2006).
20. K. J. Xu *et al.*, Metallic surface states in a correlated d-electron topological kondo insulator candidate FeSb2. *Proc. Natl. Acad. Sci. U.S.A.* **117**, 15409 (2020).
21. R. Hu, V. Mitrović, C. Petrovic, Anisotropy in the magnetic and transport properties of Fe1−xCrxSb2. *Phys. Rev. B Condens. Matter Mater. Phys.* **76**, 115105 (2007).
22. R. Hu, V. Mitrović, C. Petrovic, Anisotropy in the magnetic and transport properties of Fe1−xCoxSb2. *Phys. Rev. B Condens. Matter Mater. Phys.* **74**, 195130 (2006).
23. D. Gosálbez-Martínez, I. Souza, D. Vanderbilt, Chiral degeneracies and Fermi-surface Chern numbers in bcc Fe. *Phys. Rev. B* **92**, 085138 (2015).
24. K. Kim *et al.*, Large anomalous Hall current induced by topological nodal lines in a ferromagnetic van der Waals semimetal. *Nat. Mater.* **17**, 794–799 (2018).
25. E. Liu *et al.*, Giant anomalous Hall effect in a ferromagnetic Kagomé-lattice semimetal. *Nat. Phys.* **14**, 1125–1131 (2018).
26. A. V. Lukoyanov, V. V. Mazurenko, V. I. Anisimov, M. Sigrist, T. M. Rice, The semiconductor-to-ferromagnetic-metal transition in FeSb2. *Eur. Phys. J. B Cond. Matter Complex Syst.* **53**, 205 (2006).
27. G. Kuhn, S. Mankovsky, H. Ebert, M. Regus, W. Bensch, Electronic structure and magnetic properties of CrSb2 and FeSb2 investigated via ab initio calculations. *Phys. Rev. B Condens. Matter Mater. Phys.* **87**, 085113 (2013).
28. J. Tomczak, Thermoelectricity in correlated narrow-gap semiconductors. *J. Phys. Cond. Matter* **30**, 183001 (2018).
29. L. Šmejkal, J. Železný, J. Sinova, T. Jungwirth, Electric control of Dirac quasiparticles by spin-orbit torque in an antiferromagnet. *Phys. Rev. Lett.* **118**, 106402 (2017).
30. L. Šmejkal, J. Sinova, T. Jungwirth, Altermagnetism: A third magnetic class delimited by spin symmetry groups. arXiv [Preprint] (2021). https://arxiv.org/abs/2105.05820 (Accessed 24 September 2021).
31. W. Wu *et al.*, Nodal surface semimetals: Theory and material realization. *Phys. Rev. B* **97**, 115125 (2018).
32. W. Feng, G. Y. Guo, J. Zhou, Y. Yao, Q. Niu, Large magneto-optical Kerr effect in noncollinear antiferromagnets Mn3X (X=Rh, Ir, Pt). *Phys. Rev. B* **92**, 144426 (2015).
33. T. Higo *et al.*, Large magneto-optical Kerr effect and imaging of magnetic octupole domains in an antiferromagnetic metal. *Nat. Photonics* **12**, 73–78 (2018).
34. W. Feng *et al.*, Topological magneto-optical effects and their quantization in noncoplanar antiferromagnets. *Nat. Commun.* **11**, 118 (2020).
35. N. Sivadas, S. Okamoto, D. Xiao, Gate-controllable magneto-optic Kerr effect in layered collinear antiferromagnets. *Phys. Rev. Lett.* **117**, 267203 (2016).
36. L. Šmejkal, A. H. MacDonald, J. Sinova, S. Nakatsuji, T. Jungwirth, Anomalous Hall antiferromagnets. arXiv [Preprint] (2021). https://arxiv.org/abs/2107.03321 (Accessed 24 September 2021).
37. D. F. Shao, J. Ding, G. Gurung, S. H. Zhang, E. Y. Tsymbal, Interfacial crystal hall effect reversible by ferroelectric polarization. *Phys. Rev. Appl.* **15**, 024057 (2021).
38. G. Kresse, J. Hafner, *Ab initio* molecular dynamics for liquid metals. *Phys. Rev. B Condens. Matter* **47**, 558–561 (1993).
39. J. P. Perdew, K. Burke, M. Ernzerhof, Generalized gradient approximation made simple. *Phys. Rev. Lett.* **77**, 3865–3868 (1996).
40. P. E. Blöchl, Projector augmented-wave method. *Phys. Rev. B Condens. Matter* **50**, 17953–17979 (1994).
41. C. Petrovic, J. Kim, S. Bud'ko, A. Goldman, P. Canfield, Anisotropy and large magnetoresistance in the narrow-gap semiconductor FeSb2. *Phys. Rev. B Condens. Matter Mater. Phys.* **67**, 155205 (2003).
42. K. Koepernik, H. Eschrig, Full-potential nonorthogonal local-orbital minimum-basis band-structure scheme. *Phys. Rev. B Condens. Matter Mater. Phys.* **59**, 1743–1757 (1999).
43. P. Blaha, K. Schwarz, G. K. H. Madsen, D. Kvasnicka, J. Luitz, *Wien2k* (Vienna University of Technology, Vienna, Austria, 2002).
44. T. Koyama, H. Nakamura, T. Kohara, Y. Takahashi, Magnetization process of narrow-gap semiconductor FeSb2. *J. Phys. Soc. Jpn.* **79**, 093704 (2010).
45. I. A. Zaliznyak, A. T. Savici, V. O. Garlea, R. Hu, C. Petrovic, Absence of localized-spin magnetism in the narrow-gap semiconductor FeSb2. *Phys. Rev. B Condens. Matter Mater. Phys.* **83**, 184414 (2011).
46. U. Herath *et al.*, Pyprocar: A python library for electronic structure pre/post-processing. *Comput. Phys. Commun.* **251**, 107080 (2020).
47. G. Pizzi *et al.*, Wannier90 as a community code: New features and applications. *J. Phys. Condens. Matter* **32**, 165902 (2020).
48. Q. S. Wu, S. N. Zhang, H. F. Song, M. Troyer, A. A. Soluyanov, WannierTools: An open-source software package for novel topological materials. *Comput. Phys. Commun.* **224**, 405–416 (2017).
49. H. Eschrig, K. Koepernik, Tight-binding models for the iron-based superconductors. *Phys. Rev. B Condens. Matter Mater. Phys.* **80**, 104503 (2009).
50. X. Wang, J. R. Yates, I. Souza, D. Vanderbilt, *Ab initio* calculation of the anomalous hall conductivity by wannier interpolation. *Phys. Rev. B Condens. Matter Mater. Phys.* **74**, 195118 (2006).

Supplementary information:

Anti-Kramers antiferromagnetism in doped FeSb$_2$

I. I. Mazin,[1, 2] K. Koepernik,[3] M.D. Johannes,[4]

Rafael González-Hernández,[5, 6] and Libor Šmejkal[6, 7]

[1]*Department of Physics and Astronomy,*
George Mason University, Fairfax, USA

[2]*Center for Quantum Science and Engineering,*
George Mason University, Fairfax, USA

[3]*Institute for Theoretical Solid State Physics,*
IFW Dresden, 01069 Dresden, Germany

[4]*Center for Computational Materials Science,*
Naval Research Laboratory, Washington D.C., USA

[5]*Grupo de Investigación en Física Aplicada, Departamento de Física,*
Universidad del Norte, Barranquilla, Colombia

[6]*Institut für Physik, Johannes Gutenberg Universität Mainz, 55128 Mainz, Germany*

[7]*Institute of Physics, Czech Academy of Sciences,*
Cukrovarnická 10, 162 00, Praha 6, Czech Republic
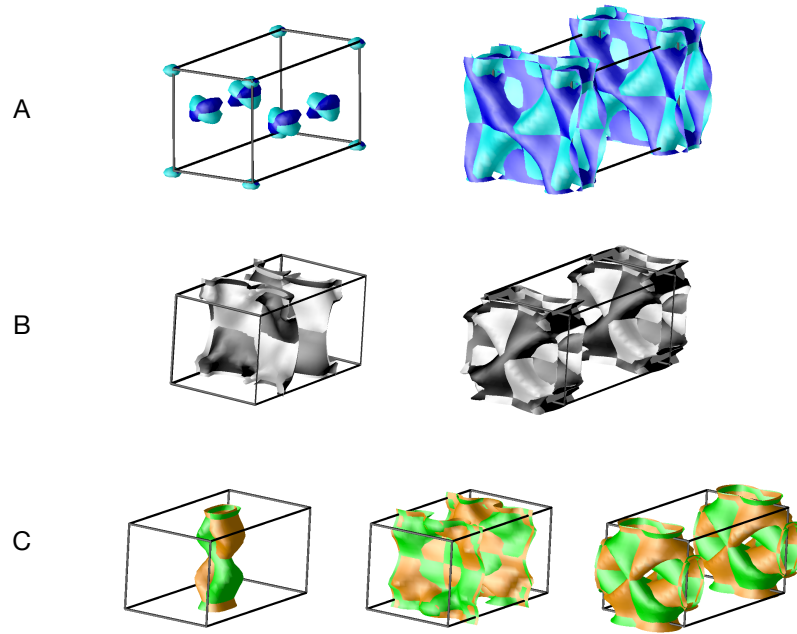
(Dated: March 31, 2021)

Figure S 1. Calculated Fermi surface pockets for: (a) $Co_{0.2}Fe_{0.8}Sb_2$, (b) $FeSb_2$, and (c) $Cr_{0.15}Fe_{0.85}Sb_2$. The orientation of the Brillouin zone is shown in panel (d). Note that number of pockets increases with the number of electrons.
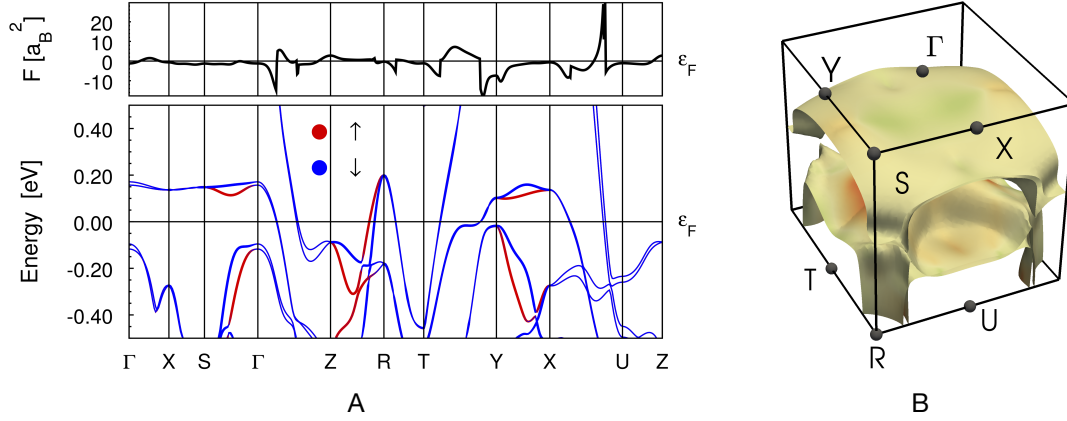
Figure S 2. (a) Calculated energy bands and Berry curvature $\mathcal{F}$ along high symmetry path in momentum space. (b) Spin polarization S_y along the [010] direction plot on top of the Fermi surface demonstrates vanishing net moment along the momenta with a large Berry curvature, cf. Fig. 4(e) in main text. The plots were calculated in the FPLO code, see Methods.?????
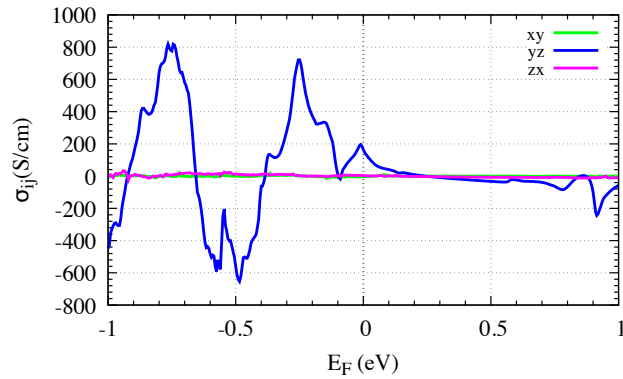

Figure S 3. Calculated spontanous intrinsic crystal Hall conductivity as a function of the Fermi energy, calculated using VASP and Wannier90 codes, for the spin direction [010]. Note that, in agreement with the symmetry analysis in the main text, the only nonzero component is σ_{yz}.

3

	ΓX	XS	SY	YΓ	ΓZ	XU	SR	YT	ZU	UR	RT	TZ
no SOC	✓	✓	✓	✓	✓	✓	✓	✓	✓	✓	✓	✓
100		✓	✓			✓	✓			✓	✓	
010		✓	✓			✓	✓				✓	✓
001	✓	✓	✓	✓	✓		✓					
arbitrary		✓	✓									

TABLE I. Spin degeneracy of high symmetry lines in the Brillouin zone without (line 2) and with (lines 3-6) spin-orbit interaction. The first column indicates the spin quantization axis for relativistic calculations.

	ΓXUZ	ΓYTZ	XSRU	SYTR	ZURT	ZURT
no SOC		✓	✓	✓	✓	
100				✓		
010					✓	
001						

TABLE II. Same as in Tab. I, for high symmetry planes .